

Contents lists available at ScienceDirect

Experimental Thermal and Fluid Science

journal homepage: www.elsevier.com/locate/etfs

Penetration depth of plunging liquid jets – A data driven modelling approach



M. Kramer, S. Wieprecht, K. Terheiden*

Institute for Modelling Hydraulic and Environmental Systems, University of Stuttgart, Germany

ARTICLE INFO

Article history:

Received 23 October 2015
 Received in revised form 18 February 2016
 Accepted 7 March 2016
 Available online 11 March 2016

Keywords:

Plunging water jet
 Penetration depth
 Air entrainment
 Artificial neural network
 Impulse turbine

ABSTRACT

In the case of impinging water jets or droplets, air entrainment processes are crucial to the casing design of hydraulic impulse turbines in the micro-hydro sector. To initiate first steps towards a precise prediction of the complex, multi-phase casing flow of impulse turbines, single aspects such as the penetration depth of impinging liquid jets have to be separated and fully understood. Existing investigations determining penetration depths are related to a very small range of flow rates and therefore show an underestimation of the penetration depth being applied to the casing flow of impulse turbines, which are generally operated at higher flow rates. For a more general description of the air entrainment process, investigations of plunging water jets within an extended flow rate range are conducted and the penetration depth is modelled using a data driven artificial neural network (ANN) approach and a non-linear regression model.

At low flow rates, experiments results are in accordance with existing studies, whereas penetration depths up to 170 cm are measured at higher flow rates. For the mathematical models to achieve a wide range applicability, a large data base is used, including published and measured data. The modelled penetration depths can be precisely verified by the performed measurements and show correct physical behaviour, even in areas without underlying data. Calculation rules, weight matrices and biases of the trained ANN are published to achieve high transparency and scientific improvement in neural modelling of penetration depths of impinging liquid jets.

© 2016 Elsevier Inc. All rights reserved.

1. Introduction

The entrainment of air caused by impinging water jets and droplets has a great impact on many technical aspects of hydraulic engineering. For example, in the field of hydraulic machinery, specifically micro-hydro impulse turbines, air entrainment and detrainment processes have a negative impact on the durability of the pipe system and on the overall efficiency of the machinery itself. Investigations on a micro-hydro impulse turbine show that penetration depth is a key parameter for the design of the turbine casing preventing air detrainment. Based on these findings, equations for an optimized casing design of micro-hydro impulse turbines are derived from Kramer et al. [1].

Measurements at large hydropower plant “Koralpe” (Austria) demonstrated that an existing equation derived from Hager [2] seems to underestimate the penetration depth in prototype plants.

During the experiments, penetrating air bubbles were observed over the whole tailwater depth, whereas the calculated results clearly showed lower penetration depths [3]. Possible explanations include the underestimation of scaling effects, which occur by disregarding dynamic similarity conditions while transferring results. When comparing different scales of machines, prototype plants have higher flow rates, implying a greater impulse of the impinging water jet and a lower density of the tailwater flow caused by increased air entrainment. Both facts lead to higher penetration depths in the prototype scale. The lack of scale independent measurement results needs to be compensated by more general descriptions.

With regard to minimizing negative consequences of air entrainment in hydraulic structures and equipment, the governing processes have to be clearly identified and air detrainment has to be prevented using optimized design right from planning stage. Aerated flows in hydraulic engineering are complex and therefore challenging to solve with analytical or numerical methods. Recent numerical based contributions in the field of air entrainment and penetration depth of plunging are given in Refs. [4–6]. However, experimental investigations are essential for validation of

* Corresponding author.

E-mail addresses: matthias.kramer@iws.uni-stuttgart.de (M. Kramer), kristina.terheiden@iws.uni-stuttgart.de (K. Terheiden).URL: <http://www.iws.uni-stuttgart.de> (K. Terheiden).

Nomenclature

\mathbf{a}^i	neural output vector	[-]	max	maximum
ANN	artificial neural network		min	minimum
\mathbf{b}^i	bias vector	[-]	n_M	number of measurements
d_0	nozzle diameter	[m]		vector of input parameters
d_j	jet diameter at plunge point	[m]	\mathbf{p}^n	vector of input parameters, normalized
f	frequency	[Hz]	Q_w	water volume flow
\mathbf{f}^i	transfer function	[-]	RSD	relative standard deviation
g	gravitational acceleration	[m/s ²]	s	standard deviation
H_p	penetration depth	[m]	u_b	bubble terminal velocity
i	layer of the neural network	[-]	v_0	jet velocity at nozzle
\dot{I}	momentum flow at plunge point	[kg m/s ²]	v_j	impinging jet velocity
K^i	number of neurons	[-]	\mathbf{W}^i	weight matrix
l_0	nozzle length	[m]	h	water level
L	number of input parameters	[-]	\bar{x}	average of 4 measurements
L_j	jet length	[m]	α	impact angle
m	mass	[kg]	β	half spread angle of the jet

numerical results and current knowledge into aerated flows relies mainly on scaled model investigations under specific flow conditions [7]. A comprehensive survey of experimental and theoretical research on gas entrainment by plunging liquid jets is given by Bin [8], while more recent investigations and insights are presented by Kiger and Duncan [9]. Based on phenomenological observations, three different air entrainment regimes (incipient entrainment, intermittent entrainment and continuous entrainment) with three main aeration mechanisms at the plunge point of impinging water jets (aeration due to surface disturbances, aeration due to boundary layer and free surface aeration into shear layer) are identified by Chirichella et al. [10] and Ervine [11], respectively. Commonly used parameters to characterise the process of air entrainment are the bubble size distribution, void fraction, entrainment rate and penetration depth. To determine those parameters, numerous empirical correlations are given throughout the literature, e.g. in Ref. [8], but due to the different experimental conditions, the data from published studies does not allow any generalized applicability.

To provide more generalized functional dependencies of the penetration depth on a wide range of flow rates and jet lengths, detailed experimental investigations are conducted. To avoid scaling effects, full-scale experiments with an extended flow rate range are essential, especially given the multiphase flow processes. For the purposes of data evaluation and assessment, a data-driven neural network model is developed within this work.

1.1. Penetration depth

The penetration depth (H_p) of a plunging free jet is defined as the distance between the liquid surface and the deepest point reached by air bubbles during the entrainment process, see Fig. 1. At this point, the velocity of the bubble equals zero and the buoyancy force becomes dominant. Throughout the transient air entrainment process, the lower limit of the bubble swarm fluctuates continuously [8]. Therefore this point is defined by a timely weighted average rather than by one fixed value.

To determine penetration depth, mainly empirical approaches based on laboratory experiments are available. Correlations are given in Ref. [12]:

$$H_p = 2.6 \cdot (v_0 \cdot d_0)^{0.7} \quad (1)$$

and in Ref. [8]:

$$H_p = 1.20 \cdot v_j^{0.77} \cdot d_0^{0.625} \cdot L_j^{-0.094} \quad (2)$$

where H_p is the penetration depth, v_0 the jet velocity at the nozzle, d_0 the nozzle diameter, d_j the jet diameter at the plunge point and L_j the jet length. The application of the equations listed above is restricted to vertical water jets, although Eq. (2) applies specifically to low velocity jets with $v_0 < 5$ m/s. The influence of the impact angle α on the penetration depth was investigated in Ref. [13], where the jet velocity at the nozzle was varied at angles of $\alpha = 45^\circ$ and 60° . The functional dependency of the penetration depth on different input parameters is given as:

$$H_p = 4.84 \cdot v_0^{0.73} \cdot d_0^{0.93} \cdot L_j^{-0.21} \cdot (\sin \alpha)^{0.73} \quad (3)$$

Another correlation including the impact angle as well as the spread angle of the jet is presented by Clanet and Lasheras [14]:

$$H_p = \frac{(1 + \tan \beta) \cos \alpha + \tan \beta \sin \alpha \cos(\alpha - \beta)}{2 \tan \beta} \frac{v_0}{u_b} d_0 \quad (4)$$

In the equations above, H_p is the penetration depth, v_0 the jet velocity at the nozzle, d_0 the nozzle diameter, L_j the jet length, α the impact angle, β the half spread angle of the jet (assumed to $\beta = 12.5^\circ$) and u_b the bubble terminal velocity.

All presented equations are based on experiments with low flow rates of few liters per second, whereas for example the average flow rate of 14 micro-hydro impulse turbines used for energy recovery in Switzerland is $Q_w = 35.4$ l/s [15]. At those signif-

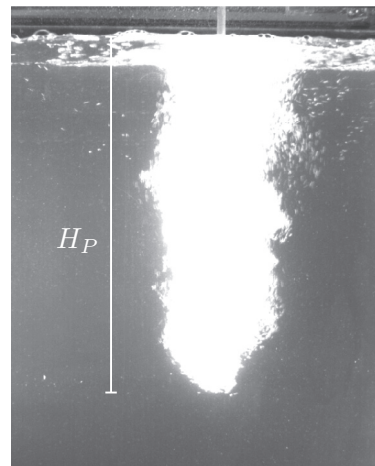


Fig. 1. Penetration depth of a plunging liquid jet.

icantly higher flow rates, the mentioned effects, such as the density reduction, are occurring in a differing order of magnitude and an application of the presented equations may underestimate the penetration depth. Therefore in order to determine the air entrainment in the tailwater of micro-hydro impulse turbines, further investigations are essential.

1.2. Artificial neural networks

Artificial neural networks (ANN) are information-processing systems with topology and working principles referring to biological neural networks. In general, artificial neural networks consist of an input and several other layers, including hidden layers and an output layer. Due the learning ability of neural networks, they are able to approximate functions of high complexity that are generally unknown. In hydraulic research of air entrainment processes, artificial neural networks have been successfully used for the prediction of oxygen transfer efficiency of weirs [16,17] and high-head conduits [18]. Furthermore, Onen [19] developed a model for the determination of penetration depths. The maximum modelled flow rate is $Q_w = 4.7$ l/s and therefore, the model is restricted in application when referring to impulse turbines.

The architecture of a neural network consisting of L scalar input parameters, a hidden layer and an output layer is illustrated in Fig. 2. The represented network is a feedforward network, meaning that nodes from one layer are only connected to the very next layer and thus information flows forward through the net. The input parameters of the illustrated network are connected to the neurons of the hidden layer via weighting factors. As the number of neurons of the hidden layer is K^1 , the weighting factors of the hidden layer is defined by the weight matrix \mathbf{W}^1 with a dimension of $K^1 \times L$.

The neural output of the first layer can be calculated with

$$\mathbf{a}^1 = \mathbf{f}^1(\mathbf{W}^1 \mathbf{p} + \mathbf{b}^1) \quad (5)$$

where \mathbf{W}^1 is the weight matrix, \mathbf{p} the vector of the input parameters, \mathbf{b}^1 a vector of biases, \mathbf{f}^1 a transfer function, and \mathbf{a}^1 the neural output of the first hidden layer. Similar to the layer weights, the biases are free parameters of the network. During the training process, weighting factors and biases are adapted in order to minimize the deviation between net output and training data. For training purposes, a variety of training algorithms are available, which are detailed extensively in Hagan et al. [20] and Zell [21]. The transfer functions shown in Fig. 2 are integral parts of artificial neural networks and are chosen depending on the particular problem. Typical transfer functions are threshold functions, sigmoid and linear functions. The net output of the presented network architecture is \mathbf{a}^2 and can be calculated as:

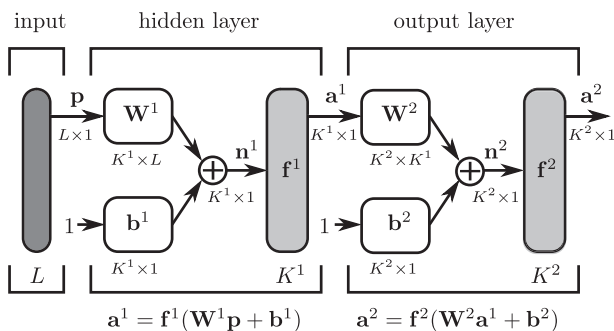


Fig. 2. Neural network architecture acc. to Ref. [20].

$$\mathbf{a}^2 = \mathbf{W}^2 \mathbf{a}^1 + \mathbf{b}^2 \quad (6)$$

$$\mathbf{a}^2 = \mathbf{f}^2(\mathbf{W}^2 \mathbf{f}^1(\mathbf{W}^1 \mathbf{p} + \mathbf{b}^1) + \mathbf{b}^2) \quad (7)$$

where \mathbf{a}^2 is the net output, \mathbf{W}^2 the weight matrix of the output layer, \mathbf{b}^2 the bias vector of the output layer and \mathbf{f}^2 the transfer function of the output layer.

2. Experiments

Fig. 3 shows the experimental setup. The experiments are performed in a $0.95 \text{ m} \cdot 0.9 \text{ m} \cdot 2.0 \text{ m}$ tank made of acrylic glass. A gate valve and electromagnetic flow meter (Q1) are located at the feeding pipe upstream of the tank. This feeding pipe is connected to a high-level tank with fixed overflow and hence constant upstream water conditions. Different nozzles with a diameter range of $d_0 = 13.0\text{--}81.9$ mm are installed at the end of the feeding pipe. During the measurements, the water level is recorded redundant using two ultrasonic sensors (h1, h2), which are installed at the top edge of the tank. In order to reduce water level fluctuations in this area, damping pipes are attached.

A second gate valve located in the outflow pipe is used for manually controlling the water level during the experiments. The pipe system is a closed circuit with the high-level tank as reservoir. For the optical measurements of penetration depth, a camera is installed within a distance of ≈ 1.8 m to the front of the tank. During measurements, the water body in the tank is illuminated evenly by a LED-spotlight. Table 1 shows a summary of the implemented measuring devices including error analysis.

2.1. Test series

Nozzle diameters (d_0), ratios of nozzle lengths and nozzle diameters (l_0/d_0), jet velocities (v_j), jet lengths (L_j) and water discharges (Q_w) of the test series are listed in Table 2. The measurements are conducted at jet velocities of $v_j = 5$ m/s or 7 m/s, which are based on precalculated velocities in the casing of impulse turbines. The jet velocity at the plunge point is assumed as

$$v_j = \sqrt{v_0 + 2gL_j} \quad (8)$$

where v_j is the jet velocity at the plunge point, v_0 is the jet velocity at the nozzle, g the gravitational acceleration and L_j the jet length. Furthermore, three different jet lengths of $L_j = 20$ cm, 60 cm and 100 cm are investigated. The jet length is chosen according to the conditions of impulse turbines, where the distance between runner and downstream water level is defining the jet length. Typically values of 1–3 m are realised in large scale arrangements, while lower values used in these investigations are common in the micro hydro sector. The water level in the tank is kept at a constant height of $h \approx 180$ cm, measured from the bottom of the tank. The detectable penetration depth clearly exceeds $H_p = 120$ cm, which was the maximum measured until now [22]. With respect to the chosen nozzle diameters, jet velocities and jet lengths, the water volume flows of the test series are of $Q_w = 0.6\text{--}35.4$ l/s. For each discharge, measurements are repeated four times ($n_M = 4$).

2.2. Experimental procedure

The experimental procedure for determination of the penetration depth is generally similar for all measurement. The selected nozzle is installed onto the feeding pipe and the required flow rate is adjusted by regulating the upstream gate valve. The water level in the tank is controlled by a downstream gate valve and remains constant from the nozzle with a distance of L_j . As soon as steady-state conditions of inflow, outflow and water level (tank) are

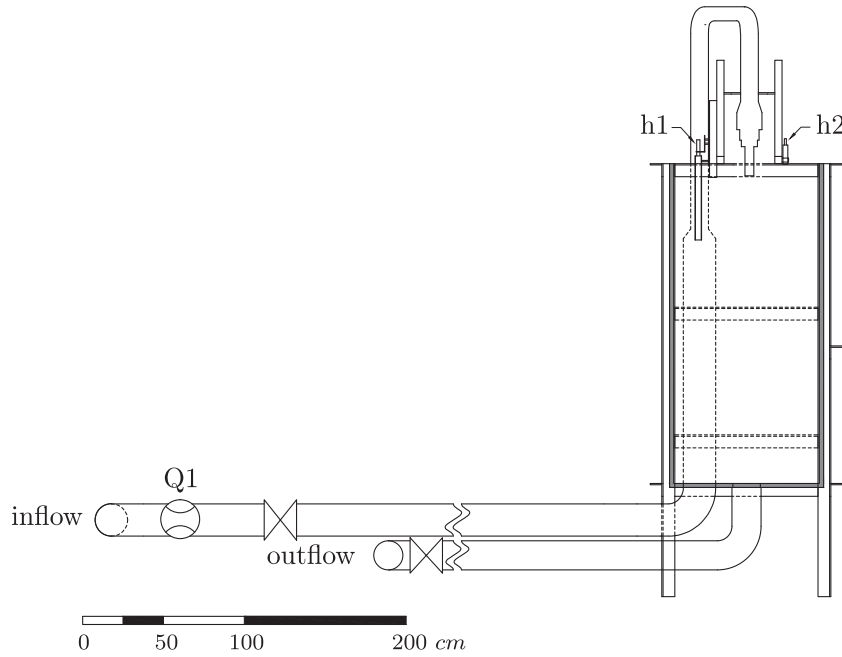


Fig. 3. Experimental setup; implemented measuring devices see Table 1.

Table 1
Implemented measurement devices in the test-bed.

Name	Device	Measured variable	Error
Q1	Krone	Discharge	±0.5%
h1	Pepperl + Fuchs UB500	Water-level	±1.0%
h2	Pepperl + Fuchs UB500	Water-level	±1.0%

Table 2
Conducted test series; $n_M = 4$.

Nr. [-]	d_0 [mm]	l_0/d_0 [-]	v_j [m/s]	L_j [cm]	Q_w [l/s]
1	13.0	4.3	5	20; 60; 100	0.6; 0.5; 0.3
2	16.5	3.4	5	20; 60; 100	1.0; 0.8; 0.5
3	20.0	2.7	5	20; 60; 100	1.4; 1.1; 0.7
4	34.0	1.9	5	20; 60; 100	4.2; 3.3; 2.1
5	44.0	2.1	5	20; 60; 100	7.0; 5.6; 3.5
6	52.5	1.9	5	20; 60; 100	9.9; 7.9; 5.0
7	68.9	1.7	5	20; 60; 100	17.1; 13.5; 8.6
8	81.9	1.5	5	20; 60; 100	24.2; 19.1; 12.2
9	13.0	4.3	7	20; 60, 100	0.9; 0.8; 0.7
10	16.5	3.4	7	20; 60, 100	1.4; 1.3; 1.2
11	20.0	2.7	7	20; 60, 100	2.1; 1.9; 1.7
12	34.0	1.9	7	20; 60, 100	6.1; 5.5; 4.9
13	44.1	2.1	7	20; 60, 100	10.3; 9.3; 8.3
14	52.5	1.7	7	20; 60, 100	14.5; 13.2; 11.7
15	68.9	1.5	7	20; 60, 100	25.0; 22.7; 20.2
16	81.9	1.5	7	20; 60, 100	35.4; 32.1; 28.5

reached, the measurement begins. The measurement time was studied in preliminary investigations with results showing that a time of $t = 60$ s is adequate to capture the penetration depth; a longer measurement time did not lead to more precise results (measured penetration depths are still fluctuating, but in a small range), while shorter times resulted in a wider spread of measured penetration depths. During measurement, the camera is focused on the bubble plume and images are taken with a frequency of $f = 2$ Hz and a resolution of 1.3 megapixels. A scale, which is attached to the front of the tank, allows for assignment of recorded heights related to the measured tank water level. The possible error due to the resolution is determined to 0.8 mm, while further errors due to

refraction and distortion are corrected by additional calibration measurements conducted with a second scale inside the water body. The overall error is estimated to be within the range of 1 cm. Images of the test series 7 with a jet length of $L_j = 20$ cm and a jet velocity of $v_j = 5$ m/s are shown in Fig. 4.

It is obvious that the process of air entrainment is highly transient: the penetration depths of the image series in Fig. 4 fluctuate in a range of several decimeters. The fluctuations are evaluated through the assessment of the minimum ($H_{p,min}$) and maximum ($H_{p,max}$) penetration depth of each measurement.

3. Results

The results of the experiments are shown in Figs. 5 and 6, where the measured penetration depths ($H_{p,max}$) are plotted against the momentum flows (\dot{I}) at the plunge point. The momentum flow is defined as:

$$\dot{I} = \dot{m} v_j = \rho Q_w v_j \quad (9)$$

where \dot{I} is the momentum flow, \dot{m} the mass flow, v_j the jet velocity at the plunge point, ρ the density and Q_w the water volume flow. The fluctuations which occur within the four repetitions are indicated with error bars and relative standard deviations (*RSD*) are listed in Table 3. As jet velocities at the plunge point are kept constant, an increase of flow rate and momentum flow is achieved by variation of the nozzle diameter. The maximum detectable penetration depth of $H_p = 180$ cm is exceeded during measurements of series 8, 15 and 16 at a jet length of $L_j = 20$ cm and during series 16 at $L_j = 60$ cm. As the bubble plume reached the bottom of the tank, those results are not plotted.

As expected, investigations results show an increase of penetration depth with increasing momentum flows and decreasing jet lengths. Maximum penetration depths up to $H_p = 170$ cm are measured in the range of higher momentum flows, which had not been investigated so far. The characteristic relationship between momentum flows and penetration depths shows a flattening at higher momentum flows. Possible primary reasons include fluid-mechanical effects such as higher entrainment rates and therefore

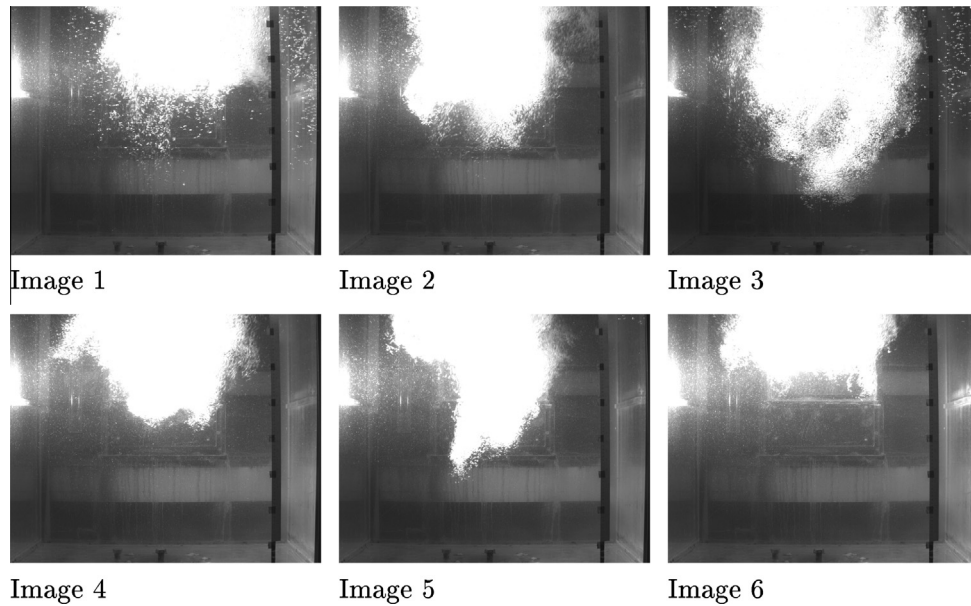


Fig. 4. Representative images of test series 7; $d_0 = 68.9$ mm; $v_j = 5$ m/s; $Q_w = 17.1$ l/s; $L_j = 20$ cm.

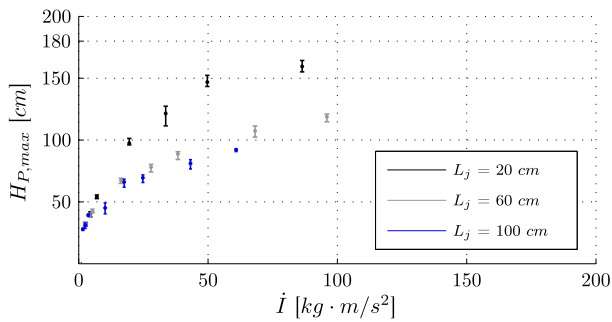


Fig. 5. Maximum penetration depths at constant jet velocity at the plunge point; $d_0 = 13.0$ – 81.9 mm; $v_j = 5$ m/s; $\alpha = 90^\circ$; $n_M = 4$.

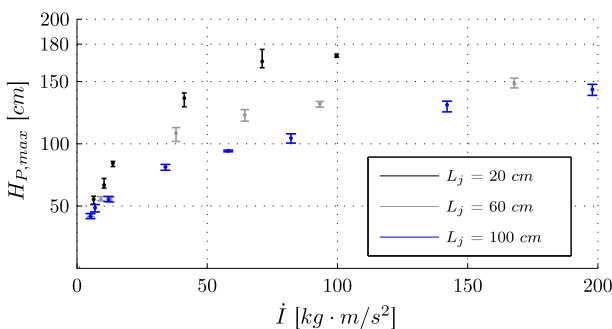


Fig. 6. Maximum penetration depths at constant jet velocity at the plunge point; $d_0 = 13.0$ – 81.9 mm; $v_j = 7$ m/s; $\alpha = 90^\circ$; $n_M = 4$.

larger buoyancy forces. Boundary effects, caused by the limited dimensions of the tank, may lead to a deceleration of the penetrating water at higher depths and can be regarded as secondary reasons for the observed behaviour. The mentioned effects may also occur in the casing of large-scale hydropower plants, where the maximum penetration depth is restricted due to the geometrical dimensions of the tailwater channel, e.g. 1.9 m at the “Koralpe” hydropower plant and 2.45 m at the “Lünersee” plant [3]. Therefore measured penetration depths represent the full range of hydropower plants, from large to micro, and confirm the flow observations in the casing of prototype plants.

Table 3

Relative standard deviations of conducted measurements.

Nr. [-]	L_j [cm]	RSD [%]	L_j [cm]	RSD [%]	L_j [cm]	RSD [%]
1	20	3.8	60	4.3	100	2.7
2	20	4.3	60	2.2	100	6.3
3	20	2.5	60	3.0	100	1.6
4	20	2.6	60	2.8	100	8.4
5	20	5.9	60	3.6	100	4.5
6	20	2.6	60	3.4	100	4.0
7	20	2.9	60	3.5	100	4.5
8	20	–	60	2.3	100	1.2
9	20	4.9	60	2.5	100	4.1
10	20	5.4	60	2.8	100	5.0
11	20	2.2	60	3.2	100	3.6
12	20	3.5	60	3.7	100	2.5
13	20	4.0	60	3.8	100	0.6
14	20	0.7	60	1.5	100	2.9
15	20	–	60	2.2	100	2.9
16	20	–	60	–	100	2.5

The relative standard deviation represents the spread of the recorded data and is a measure of the random uncertainty. The relative standard deviation is calculated as

$$RSD = s/\bar{x} \quad (10)$$

where RSD is the relative standard deviation, s the standard deviation and \bar{x} the average of 4 measurements. The relative standard deviations of the measurements are within the low single-digit range, see Table 3.

3.1. Fluctuation of penetration depth

Fig. 7 shows a comparison of maximum and minimum penetration depths measured at a jet velocity of $v_j = 5$ m/s and a jet length of $L_j = 20$ cm. It is evident that fluctuations (difference between $H_{P,max}$ and $H_{P,min}$) increase with higher momentum flows.

For instance, the fluctuation at the lowest momentum flow of $\dot{I} = 2.7$ kg m/s² is 0.9 dm, while fluctuations in a range of 3.3–3.5 dm are reached at momentum flows of $\dot{I} = 86.2$ kg m/s² and 49.7 kg m/s². This increase in the magnitude of fluctuation results

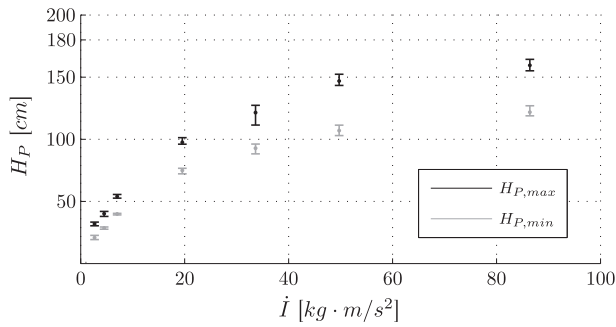


Fig. 7. Comparison between maximum and minimum penetration depths; $d_0 = 13.0\text{--}68.9$ mm; $v_j = 5$ m/s; $L_j = 20$ cm; $\alpha = 90^\circ$; $n_M = 4$.

from the transient behaviour of the air entrainment process. As larger air volumes are entrained at higher momentum flows, highly variable local velocity fields are caused due to the transient entrainment rates. This can be seen by the oscillation of the penetration depth of bubble plume at higher momentum flows.

3.2. Comparison with existing studies

In this study, the chosen range of momentum flows and flow rates of the plunging liquid jets exceeds the range published so far. Fig. 8 shows a comparison of the measured data from present experiments with the available data published by Baylar and Emiroglu [22] and Harby et al. [23]. The experimental conditions of the compared studies are given in Table 4. The measured penetration depths of the present study are in accordance with literature data at low momentum flows. Preliminary investigations undertaken with the actual experimental setup confirm the reliability of these results: measurements were conducted under the constraints of Harby's study [23] and their results could be reproduced.

At higher momentum flows, the present results show a wider spread of penetration depths. This behaviour is to be expected as air entrainment and buoyancy forces are increasing at greater jet lengths. When comparing the actual measurements with the data of Baylar and Emiroglu [22], it is obvious that the present results at $L_j = 100$ cm are in proximity to Baylar's data recorded at $L_j = 30$ cm (Table 4). These results are reasonable, owing to the incline of the jet in the study of Baylar and Emiroglu [22]; the jet angle was set to $\alpha = 45^\circ$ and 60° . However until now, the data from Baylar and Emiroglu [22] is the only data available on higher momentum flows.

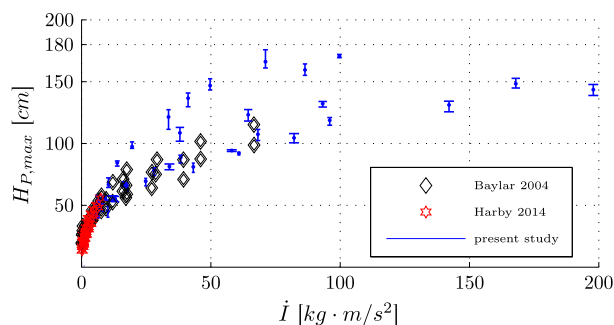


Fig. 8. Comparison of collected data and published studies [22,23].

Table 4

Experimental conditions of different studies on penetration depth of plunging jets.

Authors [-]	d_0 [mm]	v_j [m/s]	Q_w [l/s]	L_j [cm]	α [°]
Baylar and Emiroglu [22]	10, 15, 19.5	2.5–15.0	0.1–4.4	30	45, 60
Harby et al. [23]	4.0–12.0	3.5–9.9	0.1–0.9	30	90
present study	13.0–81.9	5.0, 7.0	0.3–35.4	20, 60, 100	90

4. Neural modelling

Artificial neural networks, which have already been successfully applied for prediction of parameters characterising air entrainment processes, are used to model the penetration depth of plunging liquid jets. The neural modelling is carried out using the Neural Network Toolbox in MATLAB (R2013a); the procedure can be divided into the following steps:

1. Problem description
 - Identification of input and output parameters
2. Data collection and preparation
 - Digitalization of available data from literature
 - Selection of suitable data sets
 - Division into training and test data sets
3. Model building
 - Determination of network architecture
 - Selection of training algorithm
4. Model test
 - Comparison of modelled and measured output parameters
 - Model optimization (adaption of network architecture)

4.1. Problem description

The momentum flow \dot{I} at the plunge point and the jet length L_j are chosen as input parameters for the neural network model. The measurements of this study are carried out at a constant impact angle of $\alpha = 90^\circ$. There are two main reasons justifying this. On the one hand, the impact angles in the casing of impulse turbines at optimal operating conditions are about $\alpha = 90^\circ$, while on the other hand a perpendicular impinging jet will deliver the largest penetration depth. Furthermore, only jet lengths larger than $L_j = 17.5$ cm are considered. At small distances between the runner and the tailwater, spraying water would lead to a deceleration of the runner and therefore to efficiency losses.

4.2. Data collection and preparation

The measurements results of 176 data sets are supplemented with data from Danciu et al. [24] (2009, six data sets), Qu et al. [25] (2013, 12 data sets) and Harby et al. [23] (2014, 34 data sets). In total, 228 data sets are available for training and testing the neural network. The data sets from literature have been extracted from tables or determined through digitalization of published figures. 70% of the total number of data sets are assigned randomly for training, 15% for validation and 15% for testing. This partitioning into training, validation and test data is commonly used in neural network modelling, see Ref. [20]. Table 5 shows the minimum and maximum values of the input and output parameters of the data sets. These values therefore define the application limits of the neural network. As neural networks generate their knowledge

Table 5

Application limits of the neural network.

\dot{I} [kg m/s ²]	L_j [m]	α [°]
0.1–198.5	0.175–1.01	90

from given data, an application beyond the specified data range may not lead to correct results.

4.3. Model description

The implemented neural network is a feedforward network and the architecture corresponds to Fig. 2 with $L = 2$ and $K^2 = 1$. As transfer functions, a sigmoid function ($f^1 = \tanh$) is used in the case of the hidden layer, while a linear function ($f^2 = \text{linear}$) is applied in case of the output layer. The number of neurons in the hidden layer (K^1) is optimised during model test. With the momentum flow \dot{i} (kg m/s²) and the jet length L_j (m), two parameters are included as input of the network, while the net output is given as penetration depth H_p (m). For network training, the Levenberg–Marquardt algorithm, which represents a variation of the Gauß–Newton algorithm, is applied.

4.4. Model test

The number of hidden neurons K^1 is adjusted for an optimized network architecture. As smaller networks have a better generalization ability, the optimum network is the smallest network that adequately captures the relationship in the training data [26]. To determine the optimal number of hidden neurons, an heuristic approach is used. The optimization process commences with a low number of hidden neurons and is then increased as long as there is significant improvement in the results.

In order to evaluate the performance of the neural network, the net output is compared with the penetration depths of the input data based on the coefficient of determination (R^2), the mean absolute percentage error (MAPE) and the root mean square error (RSME). Changes of the network architecture concern only the hidden layer; the input as well as the output layer remain unchanged. In Fig. 9, the performance parameters are plotted on the ordinates against the number of hidden neurons (abscissa). For each investigated number of hidden neurons, 30 networks with different initializations are trained and evaluated.

It is obvious that the error, represented by the performance parameters MAPE and RSME, decreases significantly as the number of hidden neurons increases. Simultaneously, the coefficient of determination (R^2) increases. Once above three hidden neurons, there is only a slight change in performance parameters. Therefore, the neural network with $K^1 = 3$ is chosen for the optimal architecture. In this configuration, the neural network has nine weighting factors and four biases, whose sum equals the free parameters of the approximation. An overfitting of the model during training is avoided by monitoring the errors of the validation- and test data.

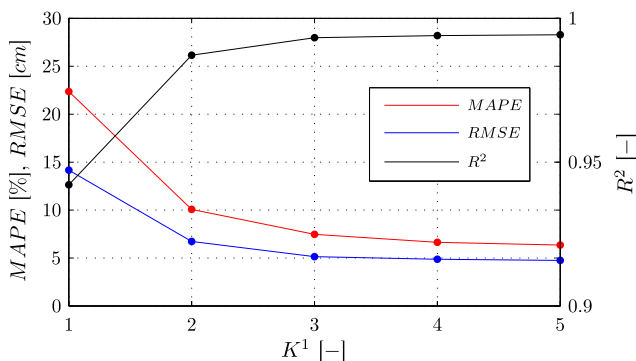


Fig. 9. Optimization of the network architecture; $n_M = 30$.

Figs. 10 and 11 show the modelled results of the trained neural network with a number of three hidden neurons. For the test, training, validation and total data, the calculated penetration depth $H_{p,cal}$ is plotted against the measured penetration depth H_p . All modelled penetration depths align with the measured penetration depths. However, to evaluate the performance of the ANN model across the full range of input parameters, which are not yet included in any data set, a raster of the input parameters \dot{i} and L_j defined in Table 5 is created and the network response is evaluated.

In Fig. 12, the calculated network response in terms of penetration depth (H_p) is plotted on the z-axis against the momentum flow (\dot{i}) on the x-axis and the jet length (L_j) on the y-axis. The underlying data (measurements) of training, test and validation are indicated as points. A distinction is made between the data of the present study (black points, typical errors and fluctuation ranges see Section 2.2) and literature data from Danciu et al. [24], Qu et al. [25] and Harby et al. [23] (red points). As already noticed, the calculated penetration depths are in accordance with measured data. Besides minimizing the error function, another crucial aspect of the model is to obtain a generalized function for problem description with correct physical behaviour. This can be achieved through a correct choice of the number of hidden neurons. Consequently, the trained model has a generalization ability for the determination of the penetration depth in the defined field of application.

In case of practical applications of that model to impulse turbines, e.g. for determination of geometrical casing dimensions according to Ref. [1], it must be taken into account that only part of the overall discharge of a turbine hits the downstream water surface directly as an impinging water jet. The remainder is dispersed onto the casing walls or with less impulse onto the water surface. Therefore, the model for determining the penetration depths represents a conservative approach in case of applications to turbines, resulting in an accurate dimensioning of the casing height of impulse turbines.

4.5. Comparison to multivariate non-linear regression

In order to evaluate the performance of the neural network, the relation between momentum flow, jet length and penetration depth is approximated with elementary functions. As a non-linear relationship between the variables is expected, a multivariate non-linear regression based on power functions is chosen and the following equation is derived:

$$H_p = a \cdot \dot{i}^b \cdot L_j^c = 0.2 \cdot \dot{i}^{0.39} \cdot L_j^{-0.26} \quad (11)$$

The model coefficients are calculated by least square regression to $a = 0.2$, $b = 0.39$ and $c = -0.26$. Penetration depths being calculated with Eq. (11) approximate the measured penetration depths accurately. However, the derived equation has higher errors in comparison to the ANN model, see Table 6. Therefore, the application of the ANN model according to Section 4.6 is recommended.

4.6. Application of the ANN model

The application of the artificial neural network model according to Ref. [20] is described within this section. The input data \dot{i} (kg m/s²) and L_j (m) are combined to an input vector \mathbf{p} :

$$\mathbf{p} = \begin{bmatrix} \dot{i} \\ L_j \end{bmatrix}$$

The input vector is normalized to a value range between -1 and 1 , and can be calculated with:

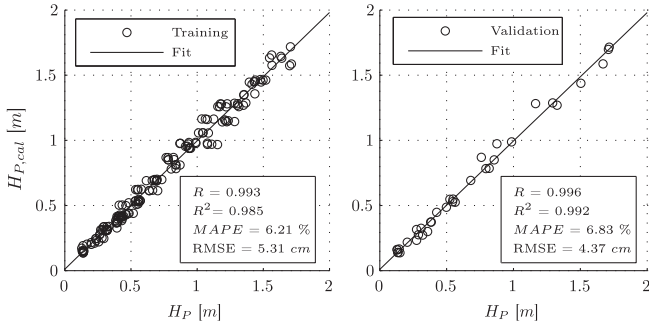


Fig. 10. Regression analysis of the modelled results; left: training data; right: validation data.

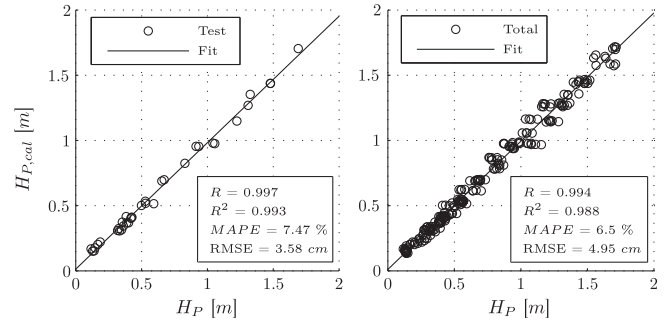


Fig. 11. Regression analysis of the modelled results; left: test data; right: total data.

$$\mathbf{p}^n = 2(\mathbf{p} - \mathbf{p}^{\min}) ./ (\mathbf{p}^{\max} - \mathbf{p}^{\min}) - 1 \quad (12)$$

where \mathbf{p}^n is the normalized input vector, \mathbf{p}^{\min} is the vector containing the minimum values of each element of the input vectors in the data sets, \mathbf{p}^{\max} contains the maximum values and the operator $./$ represents an element-by-element division of two vectors. Required specifications concerning \mathbf{p}^{\min} and \mathbf{p}^{\max} are given in Section 4.7. In the next step, the net output is calculated with:

$$\mathbf{a}^2 = \mathbf{W}^2 \tanh(\mathbf{W}^1 \mathbf{p}^n + \mathbf{b}^1) + \mathbf{b}^2 \quad (13)$$

where \mathbf{a}^2 is the net output, \mathbf{W}^1 and \mathbf{W}^2 are weight matrices, \mathbf{b}^1 and \mathbf{b}^2 are bias vectors and \mathbf{p}^n is the normalized input vector. The required weight matrices and bias vectors are given in Section 4.7, equally. To calculate the penetration depth, a reverse transformation is necessary:

$$H_P = (\mathbf{a}^2 + 1)(\mathbf{a}^{\max} - \mathbf{a}^{\min}) ./ 2 + \mathbf{a}^{\min} \quad (14)$$

where H_P is the penetration depth (m), \mathbf{a}^2 is the net output, \mathbf{a}^{\min} is the vector containing the minimum values of the output in the data sets and \mathbf{a}^{\max} contains the maximum values, see Section 4.7.

4.7. Weight matrices, biases and value ranges

The weight matrices, biases and value ranges of the trained network are shown below.

$$\mathbf{W}^1 = \begin{bmatrix} 0.2820 & 0.2816 \\ 0.2591 & 0.1969 \\ 3.1576 & 0.2542 \end{bmatrix} \quad \mathbf{W}^2 = [-23.9185 \quad 58.6958 \quad 46.9586]$$

$$\mathbf{b}^1 = \begin{bmatrix} 0.9746 \\ 1.3848 \\ 5.5941 \end{bmatrix} \quad \mathbf{b}^2 = [-80.2946]$$

$$\mathbf{p}^{\min} = \begin{bmatrix} 0.1011 \\ 0.1750 \\ 0.1162 \end{bmatrix} \quad \mathbf{p}^{\max} = \begin{bmatrix} 198.4833 \\ 1.0050 \\ 1.7160 \end{bmatrix}$$

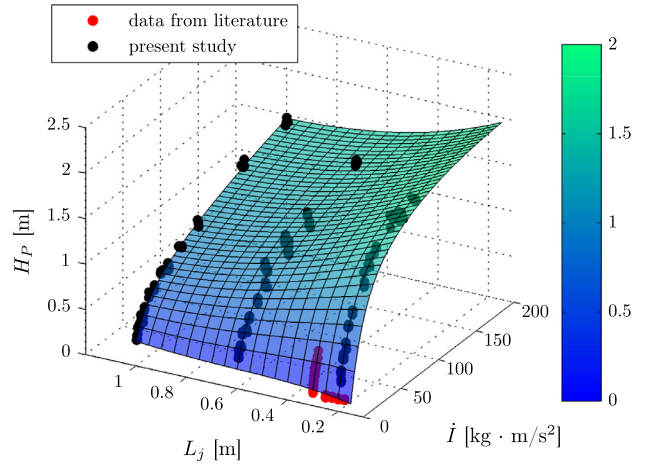


Fig. 12. Response of the ANN model; $K^1 = 3$, $\alpha = 90^\circ$ $R = 0.994$, $R^2 = 0.988$, $MAPE = 6.50\%$, $RMSE = 4.95$ cm. Literature data from Danciu et al. [24], Qu et al. [25] and Harby et al. [23].

Table 6

Comparison of different methods for the prediction of penetration depths.

Method [-]	R [-]	R^2 [-]	$MAPE$ [%]	$RMSE$ [cm]
Eq. (11)	0.988	0.971	9.79	7.56
ANN	0.994	0.988	6.50	4.95

5. Conclusion

The penetration depth of impinging water jets or droplets is a key parameter concerning the casing design of hydraulic impulse turbines preventing air detrainment. There is currently a lack of research determining and quantifying air detrainment processes caused by impinging water jets within hydraulic impulse turbines. As a result, this study has undertaken experimental investigations and mathematical modelling of the penetration depth of plunging water jets.

For experimental measurements, flow rates in a range beyond the published rates are chosen. At low flow rates, measured penetration depths are in accordance with published data. For the extended range of flow rates, penetration depths up to 170 cm are measured. These results confirm visual observations in the casing of prototype impulse turbines, where a fully mixed flow of air and water was noticed in the tailwater of the Pelton-runner.

Applying the ANN and non-linear regression approaches on the data from conducted experiments and literature meant that

predictions of the penetration depth over a wide range of momentum flow (at plunge point) and jet length became possible. The modelled penetration depths are in accordance with the study's measured results. Furthermore the resulting areal distribution of penetration depth demonstrates correct physical behaviour even in areas without underlying data. Calculation rules, weight matrices and biases of the trained network are published to achieve high transparency and to enable neural modelling of penetration depths for further applications.

Author's Contributions

Matthias Kramer and Kristina Terheiden wrote the manuscript. Matthias Kramer conducted the modelling, measurements and design of experimental setup. The data analyses and interpretation of the results were conducted by Matthias Kramer under the scientific guidance of Kristina Terheiden. The overall structure and scientific approval of this paper is done by Kristina Terheiden in cooperation with Silke Wieprecht. All authors contributed in the literature review, discussion and conclusion.

References

- [1] M. Kramer, K. Terheiden, S. Wieprecht, Optimized design of impulse turbines in the micro-hydro sector concerning air detrainment processes, *Energy J.* 93 (2015) 2604–2613.
- [2] W. Hager, Impingement basins (in German), *Österr. Wasser- und Abfallwirtschaft* 47 (1995) 91–101.
- [3] A. Arch, Air Entrainment and Detrainment Processes in Plants with Pelton Turbines in Counter Pressure Operation (in German), Ph.D. thesis, University of Graz, 2008.
- [4] X. Qu, L. Khezzer, Z. Li, The impact and air entrainment process of liquid plunging jets, *J. Process Mech. Eng.* 226 (238–249) (2012).
- [5] X. Qu, L. Khezzer, D.V. Danciu, D. Lakehal, M. Labois, Characterisation of plunging liquid jets: a combined experimental and numerical investigation, *Int. J. Multiph. Flow* 37 (7) (2011) 722–731.
- [6] L. Khezzer, N. Kharoua, Kiger, Large eddy simulation of rough and smooth liquid plunging jet processes, *Prog Nucl. Energy* 85 (2015) 140–155.
- [7] H. Chanson, Hydraulics of aerated flows: qui pro quo?, *J Hydraul. Res.* 51 (3) (2013) 223–243.
- [8] A.K. Bin, Gas Entrainment by Plunging Liquid Jets, *VDI Research Magazine* 648, Düsseldorf, 1988.
- [9] K.T. Kiger, J.H. Duncan, Air-entrainment mechanisms in plunging jets and breaking waves, *Annu. Rev. Fluid Mech.* 44 (1) (2012) 563–596.
- [10] D. Chirichella, R. Gomez Ledesma, K.T. Kiger, J.H. Duncan, Incipient air entrainment in a translating axisymmetric plunging laminar jet, *Phys. Fluids* 14 (2) (2002) 781.
- [11] D.A. Ervine, Air entrainment in hydraulic structures: a review, *Proc. Inst. Civ. Eng. – Water Marit. Energy* 130 (3) (1998) 142–153.
- [12] E.J. McKeogh, D.A. Ervine, Air entrainment rate and diffusion pattern of plunging liquid jets, *Chem. Eng. Sci.* 36 (7) (1981) 1161–1172.
- [13] T. Bagatur, Experimental analysis of flow characteristics from different circular nozzles at plunging water jets, *Arab. J. Sci. Eng.* 39 (4) (2014) 2707–2719.
- [14] C. Clanet, J.C. Lasheras, Depth of penetration of bubbles entrained by a plunging water jet, *Phys. Fluids* 9 (1997) 1864–1866.
- [15] Data Sheets of Micro-Hydro Impulse Turbines, 2015. <www.blue-water-power.ch>.
- [16] A. Baylar, D. Hanbay, E. Ozpolat, An expert system for predicting aeration performance of weirs by using ANFIS, *Expert Syst. Appl.* 35 (3) (2008) 1214–1222.
- [17] A. Baylar, K. Ozgur, M.E. Emiroglu, Modeling air entrainment rate and aeration efficiency of weirs using ANN approach, *Gazi Univ. J. Sci.* 22 (2) (2009) 107–116.
- [18] M. Unsal, D. Hanbay, Comparison of intelligent methods for predicting aeration efficiency of high-head conduits, *Kuwait J. Sci. Eng.* 39 (2B) (2012) 113–130.
- [19] F. Onen, Prediction of penetration depth in a plunging water jet using soft computing approaches, *Neural Comput. Appl.* 25 (1) (2014) 217–227.
- [20] M.T. Hagan, H.B. Demuth, H.M. Beale, O. De Jesus, *Neural Network Design*, second ed., Oklahoma, 2014.
- [21] A. Zell, *Simulation of Neural Networks* (in German), Oldenbourg Wissenschaftsverlag, 1997, ISBN 3486243500.
- [22] A. Baylar, M.E. Emiroglu, An experimental study of air entrainment and oxygen transfer at a water jet from a nozzle with air holes, *Water Environ. Res.* 76 (3) (2004) 231–237.
- [23] K. Harby, S. Chiva, J. Muñoz-Cobo, An experimental study on bubble entrainment and flow characteristics of vertical plunging water jets, *Exp. Therm. Fluid Sci.* 57 (2014) 207–220.
- [24] D.V. Danciu, M.J. da Silva, M. Schmidtke, D. Lucas, U. Hampel, Experimental investigation on air entrainment below impinging jets by means of video observations and image processing, *WIT Trans. Eng. Sci.* 63 (2009) 481–491.
- [25] X. Qu, A. Goharzadeh, L. Khezzer, A. Molki, Experimental characterization of air-entrainment in a plunging jet, *Exp. Therm. Fluid Sci.* 44 (2013) 51–61.
- [26] H.R. Maier, G.C. Dandy, Neural networks for the prediction and forecasting of water resources variables: a review of modelling issues and applications, *Environ. Model. Softw.* 15 (1) (2000) 101–124.